water

MDPI

Article

Directing Shallow-Water Waves Using Fixed Varying Bathymetry Designed by Recurrent Neural Networks

Shanran Tang, Yiqin Yang and Liangsheng Zhu *

School of Civil Engineering and Transportation, South China University of Technology, Guangzhou 510641, China; shanrantang@scut.edu.cn (S.T.)
* Correspondence: lshzhu@scut.edu.cn

Abstract: Directing shallow-water waves and their energy is highly desired in many ocean engineering applications. Coastal infrastructures can be protected by reflecting shallow-water waves to deep water. Wave energy harvesting efficiency can be improved by focusing shallow-water waves on wave energy converters. Changing water depth can effectively affect wave celerity and therefore the propagation of shallow-water waves. However, determining spatially varying bathymetry that can direct shallow-water waves to a designed location is not trivial. In this paper, we propose a novel machine learning method to design and optimize spatially varying bathymetry for directing shallow-water waves, in which the bathymetry is assumed fixed in time without considering morphodynamics. Shallow-water wave theory was applied to establish the mapping between water wave mechanics and recurrent neural networks (RNNs). Two wave-equivalent RNNs were developed to model shallow-water waves over fixed varying bathymetry. The resulting RNNs were trained to optimize bathymetry for wave energy focusing. We demonstrate that the bathymetry optimized by the wave-equivalent RNNs can effectively reflect and refract wave energy to various designed locations. We also foresee the potential that new engineering tools can be similarly developed based on the mathematical equivalence between wave mechanics and recurrent neural networks.

Keywords: shallow-water wave; wave focusing; varying bathymetry; machine learning; recurrent neural network

Citation: Tang, S.; Yang, Y.; Zhu, L. Directing Shallow-Water Waves Using Fixed Varying Bathymetry Designed by Recurrent Neural Networks. *Water* **2023**, *15*, 2414. https://doi.org/10.3390/w15132414

Academic Editors: Ruey-Syan Shih and Chia-Ming Fan

Received: 15 May 2023
Revised: 24 June 2023
Accepted: 28 June 2023
Published: 29 June 2023

1. Introduction

Directing shallow-water waves through varying bathymetry is an intriguing scientific topic that enables the control of wave energy propagation. Such wave-directing bathymetry can serve multiple purposes, including coastal protection, wave energy harvesting, and recreational surfing. In this paper, we propose a novel machine learning method to determine wave-directing bathymetry based on a type of wave-equivalent recurrent neural networks (RNNs).

Various structures have been developed for coastal protection. These structures include hard engineering solutions, such as seawalls and breakwaters [1,2], and soft ecoengineering solutions, such as artificial reefs and mangrove forests [3,4]. Submerged breakwaters, among the hard engineering structures, have minimal aesthetic and environmental impacts [5–7], and can be constructed from artificial reefs as an ecofriendly solution [8–10]. The presence of submerged breakwaters results in varying bathymetry, and it is fundamental to understand the wave–structure interactions. Li et al. [11] performed wave flume experiments to study the flow field when a solitary-like wave passed a set of submerged breakwaters. Patil and Karmakar [12], Xue et al. [13], and Jafarzadeh et al. [14] conducted two-dimensional CFD analyses in the vertical plane to evaluate the wave energy transmission over different designs of submerged breakwaters. Atras et al. [15] analytically derived the wave reflection and transmission coefficients for sinusoidal submerged breakwaters based on a half-linear shallow-water equation. Other studies on wave transmission at submerged breakwaters can be found in a comprehensive review by Brancasi et al. [16].

Analysis of the circulation in the lee of submerged breakwaters is important for coastal protection. Gallerano et al. [17] applied three-dimensional CFD simulations to study the velocity fields between submerged breakwaters and a curvilinear shoreline under the given wave conditions. Kuang et al. [18] assessed the beach evolution process behind a submerged sand bar using wave flume experiments. Ranasinghe [19] developed two Boussinesq-type nonlinear wave–current models in 2DH for impermeable and porous submerged breakwaters, respectively, to study the waves and wave-induced currents, in which a turbulence closure model is coupled to simulate wave breaking. Other researchers combined existing hydrodynamic and morphodynamic models, such as SWAN and XBeach, to study the protection performance of submerged breakwaters [20–22]. The concept of multifunctional artificial reefs has also been proposed, with the aim of improving fishing, diving, surfing, and other recreational activities, in addition to coastal protection [21]. Although extensive studies on submerged breakwaters on parametric analysis, wave–structure interaction, and performance assessment have been published, only a few are relevant to the optimization of varying bathymetry for submerged breakwaters [15,23].

Recently, the ideas of combining wave energy converters (WECs) with breakwaters [24–26] and applying wave farms for coastal protection [27] were proposed for improving efficiency and sharing costs. A varying bathymetry can be used to focus wave energy onto the places where WECs are installed to enhance energy harvesting efficiency. Deng et al. [28] demonstrated that an oscillating water column converter installed over a submerged breakwater with a proper configuration can have significantly higher energy absorption efficiency compared to a flat seafloor. Zhang et al. [29] developed a V-shape undulating bottom that enables wave focusing for energy harvesting. However, it is not trivial to design a bathymetry that directs shallow-water waves to a target location, and to the best of the authors' knowledge, there is no existing tool available for this task.

The propagation of shallow-water waves over varying bathymetry is highly complicated. A simplified shallow-water wave model is commonly applied with the shallow-water approximation (depth $\ll$ wavelength), small amplitude assumption (amplitude $\ll$ depth, wavelength), and smooth topography assumption (wavelength $\ll$ bathymetry scale), such that the wave propagation can be described by a standard 2D hyperbolic wave equation, in which the effect of water depth on wave celerity is considered but the gradient of the seafloor is neglected. On the basis of the mild-slope assumption that the relative change in bathymetry over a wavelength is small, Li [30] derived the time-dependent hyperbolic forms of the mild-slope equation. Chamberlain and Porter [31] and Porter and Staziker [32] proposed the modified mild-slope equation for improved accuracy, in which the square term of the seafloor gradient and the second derivative of bathymetry are considered. Suh et al. [33] and Lee et al. [34] derived the time-dependent hyperbolic forms of the modified mild-slope equation and applied the resulting equations to study random waves over varying bathymetry.

Boussinesq approximations are also widely used to study shallow-water waves; they assume that the square of the ratio between depth and wavelength is of the same order as the ratio between wave amplitude and depth, and both are small values. Many researchers have contributed to developing modified Boussinesq wave models to improve dispersive properties [35–37] and nonlinearities [38–40]. Boussinesq-type models are applied to simulate shallow-water waves over varying bathymetry. Madsen et al. [41] derived a high-order Boussinesq-type formulation enabling nonlinear wave simulations over rapidly varying bathymetry. Gao et al. [42,43] numerically investigated the influences of bathymetry on oscillations in a rectangular harbor using a fully nonlinear Boussinesq model named FUNWAVE.

Bragg resonance plays an important role in the interaction between shallow-water waves and bathymetry. Yu and Howard [44] studied the Bragg reflection of linear waves over periodic seafloors. Tao et al. [45] performed wave flume experiments and demonstrated the wave-focusing effect resulting from Bragg resonance. Elandt et al. [46] designed a set of seafloor ripples based on Bragg reflection to focus wave energy. Gao et al. [47] studied the effects of Bragg reflection caused by a set of sinusoidal bars for harbor os-

cillation and protection. Hao et al. [48] designed a parabolic-type bathymetry based on the characteristics of the parabolic mirror and Bragg resonance for wave energy focusing. Liu [49] investigated the Bragg resonance of linear shallow-water waves caused by five types of periodic artificial bars and proposed an approximated law for the phenomenon.

Bathymetry evolves with time due to the impacts of waves, tides, currents, and extreme events like tsunamis and storms [50]. Particularly for sandy or muddy seafloors, bathymetry interacts with shallow-water waves through the effects of wave shoaling, wave breaking, wave-induced currents, and sediment transport. Therefore, morphodynamic modeling of bathymetry evolution should include dynamics of sediment transport and hydrodynamics of waves, currents, and wave–current interactions [51–54]. Marino et al. [55] and Faraci et al. [56] experimentally investigated the orthogonal wave–current interactions over a sloping planar beach and two rough beds, respectively. Ozkan et al. [57] reviewed several studies on the coastal morphodynamics behind wave energy farms and concluded that WECs generally mitigate coastal erosion. Franzen et al. [58] reviewed five engineering applications worldwide and found that the hydro-morphodynamic effects of coastal structures are complicated: sedimentary and morphological alterations vary in magnitude and depend on local dynamics. Goldstein et al. [59] reviewed a wide range of applications of machine learning techniques for sediment transport and morphodynamic modeling.

In this study, the effects of water depth and gradient of the seafloor on wave propagation, such as reflection and refraction, are considered, while nonlinear hydrodynamic effects, such as wave breaking, are neglected since the amplitude of the incident waves is assumed to be small. Furthermore, we focus on the effects of varying bathymetry on wave propagation and confine this study without considering the evolution of bathymetry over time because its time scale is much larger than wave motion. Therefore, sediment transport and morphodynamic effects are neglected.

Machine learning is advancing rapidly and being applied to many disciplines. Two of the most successful examples are applying convolutional neural networks to computer vision [60] and applying RNNs to natural language processing [61]. Artificial neural networks are also applied for wave energy harvesting. Bento et al. [62] used the moth–flame optimization algorithm to configure the neural network structure and input data selection, and then proposed an optimized deep neural network that outperforms statistical and physics-based approaches for wave energy forecasting. Zhu et al. [63] proposed an optimization method for the layout of WEC arrays that combines a neural network model with an adaptive genetic algorithm and employed a MATLAB-AQWA simulator for power computation. Lin et al. [64] employed a neural network to replace the traditional hydrodynamic simulation tool for optimizing the buoy shape that captures the most wave energy while minimizing the current drag. Other related works can be referred to in reviews [65,66] and the references therein. Neural networks have been applied to tackle wave energy problems but the network models themselves do not explicitly embody physical meanings and generally can be modified freely to fit applications. Until recently, Hughes and Williamson et al. [67] identified the mathematical mapping between the dynamics of sound waves and the computations of RNNs. Based on the mapping between sound waves and RNN models, they proposed a type of analog machine learning hardware that can perform vowel classification on audio signals more efficiently than their digital counterparts.

We are inspired by the work of Hughes and Williamson but with different objectives. Here in this study, we aim to exploit the equivalence between wave dynamics and RNN models to develop a novel machine learning method for engineering designs. Particularly, we propose a new class of RNN to represent shallow-water waves and use it to design and optimize varying bathymetry for directing wave energy. The feedforward in time of the proposed RNN model is equivalent to the propagation of shallow-water waves. One of the weight matrices in the wave-equivalent RNN model is a function of water depth, such that the water depth is updated along with the neural network in each training epoch after conducting the backpropagation through time. Using the proposed training setup, we are

able to combine water wave computation and bathymetry optimization together within the training process of the wave-equivalent RNN model. Different design objectives can be achieved by applying various training setups, which is a significant improvement over the traditional design method of trial and error. We expect the application of wave-equivalent RNN for wave energy directing will inspire new development of intelligent engineering tools and lead to new studies on physics-equivalent neural networks.

In the remainder of this paper, we first briefly review the work of Hughes and Williamson and then introduce the proposed RNN model with the training setups for wave directing in Section 2. The training results are presented and discussed in Section 3, including limitations and CFD verification. The key findings and possible future improvements are concluded in Section 4.

2. Materials and Methods

2.1. Computation of RNN

The computation of an RNN and how that relates to wave dynamics is briefly introduced here, and more details can be found in [67]. The feedforward in time of a typical RNN can be computed using the update and output equations, Equations (1) and (2):

$$\boldsymbol{h}_T = \sigma^{(h)}\left(\boldsymbol{W}^{(h)}\cdot\boldsymbol{h}_{T-1} + \boldsymbol{W}^{(x)}\cdot\boldsymbol{x}_T\right); \tag{1}$$

$$\boldsymbol{y}_T = \sigma^{(y)}\left(\boldsymbol{W}^{(y)}\cdot\boldsymbol{h}_T\right), \tag{2}$$

in which $\boldsymbol{h}_T$ and $\boldsymbol{h}_{T-1}$ are the hidden states of the neural network at time steps T and $T-1$, respectively; $\boldsymbol{x}_T$ is the input vector of the RNN; $\boldsymbol{y}_T$ is the output vector; $\sigma^{(h)}(\ )$ and $\sigma^{(y)}(\ )$ are activation functions; and $\boldsymbol{W}^{(h)}$, $\boldsymbol{W}^{(x)}$, and $\boldsymbol{W}^{(y)}$ are the weight matrices that are updated in every training epoch.

On the other hand, the dynamics of a scalar wave field generally can be described by a hyperbolic partial differential equation, Equation (3):

$$\frac{\partial^2 u}{\partial t^2} - c^2\nabla^2 u = f, \tag{3}$$

where $u(x, y, z, t)$ is the scalar field variable; $c(x, y, z)$ is the wave speed; ∇^2 is the Laplacian operator; and $f(x, y, z, t)$ is the source term that excites the wave field. Applying the finite difference method to Equation (3) in time domain, the wave equation can be discretized with a time-step size of Δt and formulated in a matrix form as Equation (4):

$$\begin{bmatrix} u_{t+1} \\ u_t \end{bmatrix} = \begin{bmatrix} 2+\Delta t^2 c^2\nabla^2 & -1 \\ 1 & 0 \end{bmatrix}\cdot\begin{bmatrix} u_t \\ u_{t-1} \end{bmatrix} + \Delta t^2\begin{bmatrix} f_t \\ 0 \end{bmatrix}. \tag{4}$$

To relate the computation of an RNN with the wave equation, we set the hidden state $\boldsymbol{h}_T = \begin{bmatrix} u_{t+1} \\ u_t \end{bmatrix}$ and consider that the input vector $\boldsymbol{x}_T$ is a function of the source term f_t. Then, Equation (4) can be expressed as Equation (5):

$$\boldsymbol{h}_T = \boldsymbol{A}\cdot\boldsymbol{h}_{T-1} + \boldsymbol{P}^{(i)}\cdot\boldsymbol{x}_T, \tag{5}$$

in which matrix $\boldsymbol{A} = \begin{bmatrix} 2+\Delta t^2 c^2\nabla^2 & -1 \\ 1 & 0 \end{bmatrix}$ is equivalent to the weight matrix $\boldsymbol{W}^{(h)}$, and $\boldsymbol{P}^{(i)}$ is equivalent to the weight matrix $\boldsymbol{W}^{(x)}$. Matrix $\boldsymbol{A}$ can be a function of $\boldsymbol{h}_{T-1}$ for nonlinear waves if the wave speed c is dependent on the scalar wave field. Equations (1) and (5) are mathematically equivalent if the activation function is neglected. Similarly, the output equation equivalent to Equation (2) can be written as Equation (6):

$$\boldsymbol{y}_T = \boldsymbol{P}^{(o)}\cdot\boldsymbol{h}_T, \tag{6}$$

in which $\boldsymbol{P}^{(o)}$ is the extraction matrix that extracts output values from the wave field and is equivalent to the weight matrix $\boldsymbol{W}^{(y)}$.

Further applying spatial discretization to Equations (5) and (6), the hidden state becomes a vector whose components are the discretized values of u in the wave field. Then, a wave-equivalent RNN model can be developed based on Equations (5) and (6) to represent a physical wave system.

2.2. Equations of Shallow-Water Waves

For shallow-water waves, water depth H is considered to be small compared to wavelength L, i.e., $\frac{H}{L} \leq \frac{1}{20}$, such that the dispersion relationship is simplified as Equation (7):

$$\omega = k\sqrt{gH}, \tag{7}$$

and the phase velocity c and group velocity c_g are computed by Equation (8):

$$c = c_g = \sqrt{gH}, \tag{8}$$

in which $\omega = \frac{2\pi}{T}$ is wave frequency; $k = \frac{2\pi}{L}$ is wave number; and g is the gravitational acceleration.

Surface elevation $\eta(x, y, t)$ of shallow-water waves can be described by the simplified shallow-water wave equation, Equation (9), if the gradient of bathymetry is neglected under shallow water, small amplitude, and smooth topography assumptions:

$$\frac{\partial^2 \eta}{\partial t^2} - gH\nabla^2\eta = 0. \tag{9}$$

When the gradient of bathymetry is considered, one can employ the mild-slope equation whose hyperbolic form [30] is given by Equation (10):

$$\frac{\partial^2 \eta}{\partial t^2} - \nabla\cdot(cc_g\nabla\eta) + (\omega^2 - k^2cc_g)\eta = 0. \tag{10}$$

Equation (10) can be reduced to Equation (11) for shallow water, combining Equations (7) and (8):

$$\frac{\partial^2 \eta}{\partial t^2} - \nabla\cdot(gH\nabla\eta) = 0. \tag{11}$$

For the modified mild-slope equation, its hyperbolic form was derived with respect to velocity potential by Suh et al. [33] and was rewritten with respect to η by Lee et al. [34] as Equation (12):

$$\frac{\partial^2 \eta}{\partial t^2} - \nabla\cdot(cc_g\nabla\eta) + (\omega^2 - k^2cc_g)\eta + \omega^2\left[R_1(\nabla H)^2 + R_2\nabla^2 H\right]\eta = 0, \tag{12}$$

in which R_1 and R_2 are the second-order effect coefficients associated with the square term of the bottom gradient and the second derivative of bathymetry, respectively. R_1 and R_2 are functions of k and H, whose formulations are given by Equations (13) and (14):

$$R_1 = \frac{sech^2\ kH}{4(2kH + sinh\ 2kH)}(sinh\ 2kH - 2kH\ cosh\ 2kH), \tag{13}$$

$$\begin{aligned} R_2 = \frac{k\ \mathrm{sech}^2\ kH}{12(2kH+\sinh\ 2kH)^3}[&(2kH)^4 + 4(2kH)^3\sinh\ 2kH - 9\ \sinh\ 2kH\ \sinh\ 4kH \\ &+6kH(2kH + \sinh\ 2kH)(\cosh^2\ 2kH - 2\cosh 2kH + 3)]. \end{aligned} \tag{14}$$

2.3. Wave-Equivalent RNN Model

Equations (9) and (11) are discretized in the 2D space domain and in time domain using the finite difference method. The resulting discretized equations are converted into

the recurrent update formulation as Equation (5) to establish a wave-equivalent RNN model using the PyTorch machine learning package. Different from conventional RNNs, only matrix $\boldsymbol{A}$ is updated in each training epoch, and no activation function is applied as both the wave and RNN models are linear. Because $\boldsymbol{A}$ is a function of varying bathymetry $H(x, y)$, we essentially train the equivalent RNN model to optimize varying bathymetry for wave energy directing.

2.3.1. Recurrent Update Equation

We take the hyperbolic mild-slope equation for shallow water as an example to illustrate the derivation of the recurrent update equation. Adding the linear viscous damping and the source term in Equation (11), we obtain Equation (15):

$$\frac{\partial^2 \eta}{\partial t^2} + 2b\frac{\partial \eta}{\partial t} - g\nabla H \cdot \nabla \eta - gH\nabla^2 \eta = f, \tag{15}$$

in which b is the damping coefficient. Discretizing Equation (15) using central finite difference in time gives Equation (16):

$$\eta_{t+1} = \frac{1}{1+b\Delta t}[2\eta_t + (b\Delta t - 1)\eta_{t-1} + g\Delta t^2(\nabla H \cdot \nabla \eta_t + H\nabla^2 \eta_t)] + \Delta t^2 f_t. \tag{16}$$

The matrix form of Equation (16) is given as Equation (17):

$$\begin{bmatrix} \eta_{t+1} \\ \eta_t \end{bmatrix} = \begin{bmatrix} \frac{2+g\Delta t^2\left(\nabla H \cdot \nabla + H\nabla^2\right)}{1+b\Delta t} & \frac{b\Delta t-1}{1+b\Delta t} \\ 1 & 0 \end{bmatrix} \cdot \begin{bmatrix} \eta_t \\ \eta_{t-1} \end{bmatrix} + \Delta t^2 \begin{bmatrix} f_t \\ 0 \end{bmatrix}. \tag{17}$$

If the $\nabla H \cdot \nabla \eta_t$ term in Equation (17) is neglected, then we obtain the recurrent update equation for the simplified shallow-water wave model of Equation (9).

2.3.2. Discretized Wave Field

We spatially discretize a 2D wave field and define a new class of RNN for shallow-water waves in PyTorch. Figure 1 shows the rectangular wave field, which is discretized into N by M grids. The hidden state is defined by Equation (18) after spatial discretization:

$$\boldsymbol{h}_T = \begin{bmatrix} \boldsymbol{\eta}_{t+1} \\ \boldsymbol{\eta}_t \end{bmatrix} = \left[\eta_{t+1}^{11}, \cdots, \eta_{t+1}^{1N}, \eta_{t+1}^{21}, \cdots, \eta_{t+1}^{MN}, \eta_t^{11}, \cdots, \eta_t^{1N}, \eta_t^{21}, \cdots, \eta_t^{MN}\right]^T, \tag{18}$$

in which the superscripts indicate the spatial location in the 2D wave field.

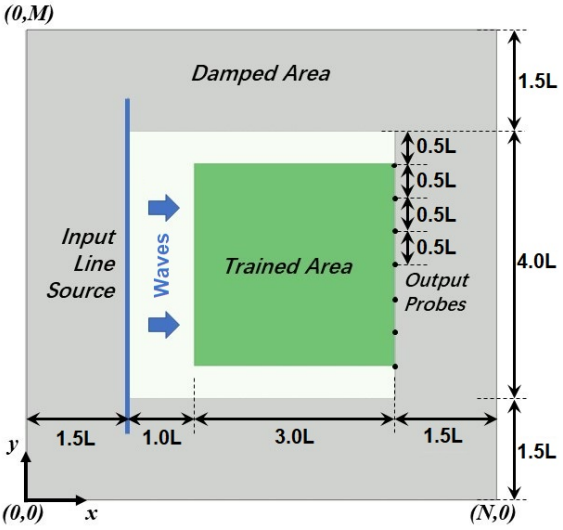

Figure 1. The 2D wave field formulated by an equivalent RNN model.

The weight matrix $\boldsymbol{A}$ associated with the hidden state is defined as Equation (19):

$$\boldsymbol{A} = \begin{bmatrix} \boldsymbol{A}_1 & \mathrm{diag}\left(\frac{-1+\Delta t b^{11}}{1+\Delta t b^{11}}, \cdots, \frac{-1+\Delta t b^{MN}}{1+\Delta t b^{MN}}\right) \\ \boldsymbol{I} & \boldsymbol{0} \end{bmatrix}. \tag{19}$$

in which:

$$\boldsymbol{A}_1 = \mathrm{diag}\left(\frac{2}{1+\Delta t b^{11}}, \cdots, \frac{2}{1+\Delta t b^{MN}}\right) + \mathrm{diag}\left(\frac{g \cdot t^2}{1+\Delta t b^{11}}, \cdots, \frac{g \cdot t^2}{1+\Delta t b^{MN}}\right) \cdot \left\{ \mathrm{diag}([\nabla] \cdot [H^{11}, \cdots, H^{MN}]^T) \cdot [\nabla] + \mathrm{diag}(H^{11}, \cdots, H^{MN}) \cdot [\nabla^2] \right\}; \tag{20}$$

$\boldsymbol{I}$ is an MN by MN identity matrix; diag( ) denotes the diagonal square matrix of a vector; and $[\nabla]$ and $[\nabla^2]$ are derivative matrices that apply spatial derivation to a 2D scaler tensor, whose components are dependent on the finite difference scheme being used. The damping coefficient vector $\boldsymbol{b} = \left[b^{11}, \cdots, b^{MN}\right]^T$ is constant, such that the only varying term in matrix $\boldsymbol{A}$ is the water depth vector $\boldsymbol{H} = \left[H^{11}, \cdots, H^{MN}\right]^T$. The damping coefficients are nonzero only in the outer damped region (the gray area in Figure 1) to avoid boundary reflection. The calculation of the damping coefficient is presented in Section 2.4.3.

Water depth should only vary in the trained area and remain unchanged in the rest of the wave field. Therefore, we introduce the pseudo water depth $\widetilde{\boldsymbol{H}} = \left[\widetilde{H}^{11}, \cdots, \widetilde{H}^{MN}\right]^T$ to limit the varying bathymetry to the trained area. Actual water depth is computed based on the pseudo water depth and the sigmoid function using Equation (21):

$$H^{ij} = H_1 + H_2 \cdot \mathrm{sigmoid}\left(\widetilde{H}^{ij}\right) = H_1 + \frac{H_2}{1 + e^{-\widetilde{H}^{ij}}}, \tag{21}$$

in which i and j are integer indices representing spatial locations; constant H_1 represents the minimum depth; constant H_2 is the varying range of depth; and $H_1 + H_2$ gives the maximum depth. When the value of pseudo depth $\widetilde{H}^{ij}$ nears zero, the gradient of its sigmoid function has meaningful values; when $\widetilde{H}^{ij}$ approaches $\pm\infty$, the gradient of its sigmoid function approaches zero (see Figure 2). In the latter case, the backpropagation algorithm would not be able to update the pseudo depth because of the vanishing gradient, and therefore the actual water depth would remain unchanged. For the initial condition, we set the pseudo depth in the trained area equal to zero and in the rest of the wave field equal to 1×10^8, such that the actual water depth is updated only within the trained area and is always equal to $H_1 + H_2$ in the rest area.

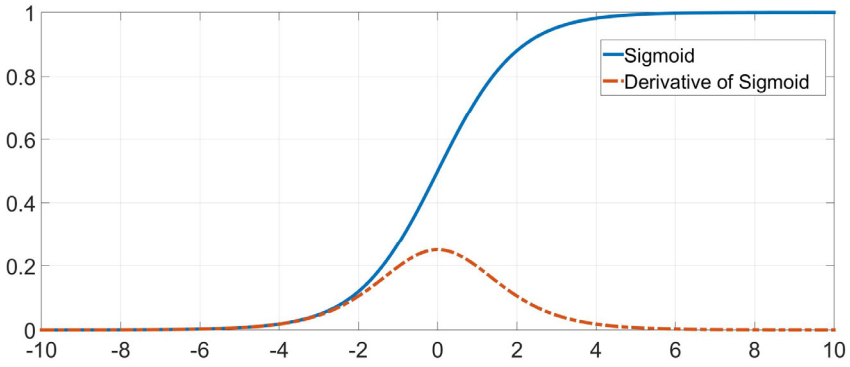

Figure 2. Value and gradient of the sigmoid function.

2.3.3. Inputs and Outputs

The input vector is defined by Equation (22) as the surface elevations at the location of a line source that generates a regular sinusoidal incident wave propagating from left to right across the wave field (Figure 1):

$$\boldsymbol{x}_T = \begin{bmatrix} \boldsymbol{f}_t \\ \boldsymbol{0} \end{bmatrix} = \left[f_t^{11}, \cdots, f_t^{1N}, f_t^{21}, \cdots, f_t^{MN}, 0, \cdots, 0 \right]^T, \tag{22}$$

in which

$$f_t^{ij} = \begin{cases} c_0 \sin \omega t, & i = c_1,\ c_2 \le j \le c_3 \\ 0, & otherwise \end{cases}; \tag{23}$$

c_0 and ω are constants that determine the wave amplitude and frequency of the incident wave; c_1, c_2, and c_3 are constants that determine the location of the input line source. The weight matrix $\boldsymbol{P}^{(i)}$ is not used in this study since the surface elevations at the input locations are directly employed as the input vector.

In this study, we place output probes at the selected locations and use Equation (24) to extract the surface elevations at these locations as the output vector of the RNN:

$$\boldsymbol{y}_T = \boldsymbol{P}^{(o)} \cdot \begin{bmatrix} \boldsymbol{\eta}_{t+1} \\ \boldsymbol{\eta}_t \end{bmatrix} = \begin{bmatrix} P_1^{11}, \cdots, P_1^{MN}, 0, \cdots, 0 \\ \vdots \\ P_K^{11}, \cdots, P_K^{MN}, 0, \cdots, 0 \end{bmatrix} \left[\eta_{t+1}^{11}, \cdots, \eta_{t+1}^{MN}, \eta_t^{11}, \cdots, \eta_t^{MN} \right]^T, \tag{24}$$

in which

$$P_k^{ij} = \begin{cases} 1, & i = X_k, j = Y_k \\ 0, & otherwise \end{cases}; \tag{25}$$

k is an integer index; K is the number of output probes; and constants X_k and Y_k determine the location of the k-th output probe.

Equations (18)–(25) are the fundamental equations used to develop the new class of RNN for shallow-water waves in PyTorch. PyTorch provides the *autograd* function that computes gradients following the chain rule as long as the feedforward computations are defined, which enables the easy implementation of backpropagation through time for the new RNN class. The wave-equivalent RNN model updates the pseudo water depth for the complete wave field after each training epoch, but only effectively changes the bathymetry in the trained area. The equivalent RNN model can be trained with various training setups to obtain different optimized bathymetry according to design objectives.

2.4. Training Setups

2.4.1. Initial Conditions and Training Target

We set $\boldsymbol{h}_{T=0} = \boldsymbol{0}$ as the initial condition for the wave field. Because the pseudo water depth is initially set to zero in the trained area and 1×10^8 in other areas, the initial water depth is $H_1 + 0.5H_2$ in the trained area and $H_1 + H_2$ otherwise.

The output time histories of surface elevations at the output probes are squared and integrated over time using Equation (26) to compute the accumulated energies at these probe locations:

$$\boldsymbol{y} = \begin{bmatrix} y_1 \\ \vdots \\ y_K \end{bmatrix} = \begin{bmatrix} \int_0^T \text{sigmoid}(t - T_0) \cdot \left(\eta_t^{X_1 Y_1} \right)^2 \cdot dt \\ \vdots \\ \int_0^T \text{sigmoid}(t - T_0) \cdot \left(\eta_t^{X_K Y_K} \right)^2 \cdot dt \end{bmatrix}, \tag{26}$$

in which T_0 is the starting time of sampling. The application of sigmoid$(t - T_0)$ in Equation (26) allows truncating the wave series before T_0 without undermining the *autograd* function in PyTorch. We choose T_0 as the time when the complete wave field is fully populated with incident wave, such that the computation of accumulated energy would not be affected by the variation in distance between the line source and output probes. The accumulated energy vector is further normalized to obtain the energy distribution among the output probes: $\overline{\boldsymbol{y}} = [\overline{y}_1, \cdots, \overline{y}_K]^{\mathrm{T}} = \frac{1}{\sum_{k=1}^{k=K} y_k} [y_1, \cdots, y_K]^{\mathrm{T}}$ and $0 \le \overline{y}_k \le 1$.

In order to focus wave energy on a designed location, we need to place one of the output probes at the designed location and set the training target as a one-hot vector: $\boldsymbol{y}_{\text{target}} = [U_1, \cdots, U_K]^{\text{T}}$, in which $U_k = 1$ if the k-th output probe is the selected focal point; otherwise, $U_k = 0$.

2.4.2. Loss Function and Optimization

We employ the negative log-likelihood loss function offered in the PyTorch package, *torch.nn.NLLLoss(input, target)*, to compute the loss value using $\overline{\boldsymbol{y}}$ as the *input* and $\boldsymbol{y}_{\text{target}}$ as the *target*. The loss value of our particular training setup is a negative scalar between 0 and -1. Perfect wave focusing would be achieved if the loss value reaches -1, which means the energy distributing among all output probes is 100% concentrated at the target focal point.

We employ the root mean square propagation (RMSprop) optimizer in PyTorch (*torch.optim.RMSprop*) to train the wave-equivalent RNN. RMSprop is a backpropagation-through-time algorithm developed based on the stochastic gradient descent algorithm, Adam optimization algorithm, and the momentum method. Essentially, in the proposed training setup, the optimizer computes the gradients of the loss value with respect to the pseudo water depth $\widetilde{\boldsymbol{H}}$ and updates $\widetilde{\boldsymbol{H}}$ to minimize the loss value (approaching to -1), which yields the optimized varying bathymetry in the trained area for wave focusing. Detailed equations and discussions on the loss function and optimization algorithm are available in PyTorch documentation [68] and are beyond the scope of this paper.

2.4.3. Model and Training Parameters

The wave field modeled is a $7L \times 7L$ rectangle with a $3L \times 3L$ square trained area inside. The grid size is selected as $\frac{L}{40}$, such that $N = M = 280$. Seven default output probes are placed on the right edge of the trained area. Additional probes can be freely added in any location within the wave field based on research or design purpose. Other detailed sizes are presented in Figure 1.

The incident wave height is set to 0.05 m ($c_0 = 0.025$ m) and water depth can vary between 0.5 m to 0.3 m in the trained area ($H_1 = 0.3$ m, $H_2 = 0.2$ m), which are also applied to the other five cases in this section. To eliminate the reflection from the boundaries, the damping coefficients of each grid are computed using Equation (27):

$$b^{ij} = \begin{cases} \sqrt{{b_x^i}^2 + {b_y^j}^2}, & i \le 60 \text{ or } i \ge 220,\ j \le 60 \text{ or } j \ge 220 \\ 0, & \text{otherwise} \end{cases} \tag{27}$$

in which

$$b_x^i = \begin{cases} 10 \cdot \left(\frac{60-i}{60}\right)^4, & i \le 60 \\ 10 \cdot \left(\frac{i-220}{60}\right)^4, & i \ge 220 \end{cases}; \tag{28}$$

$$b_y^j = \begin{cases} 10 \cdot \left(\frac{60-j}{60}\right)^4, & j \le 60 \\ 10 \cdot \left(\frac{j-220}{60}\right)^4, & j \ge 220 \end{cases}. \tag{29}$$

The wavelength $L = 10$ m is considered, which is 20 times the depth ($H_1 + H_2 = 0.5$ m). The resulting period of the shallow-water waves is $T = 4.588$ s ($\omega = 1.369$ rad/s). The time-step size is selected as $\Delta t = \frac{T}{60}$. The total simulation time is $20T$, and the starting time of sampling is set to $T_0 = 7T$.

The learning rate employed is determined by training tests. It has been found that the best learning rates yielding the best wave-focusing results for various cases are around 1, which is much higher than that of traditional neural networks. We expect that the absence of an activation function and the linear nature of the wave and RNN models are the reasons such a large learning rate can be effectively applied.

2.5. Workflow

Figure 3 shows an example of the overall workflow for the proposed method. In each training epoch, the training process includes the following steps: (a) a regular incident shallow-water wave is generated by a series of inputs and propagates over the varying bathymetry for $20T$; (b) the time histories of surface elevation at the output probes are integrated for the last $14T$ and normalized to compute the relative wave energy distribution among output locations; (c) the negative log-likelihood loss function and RMSprop optimizer are invoked to compute the loss value and update the pseudo water depth for the next epoch.

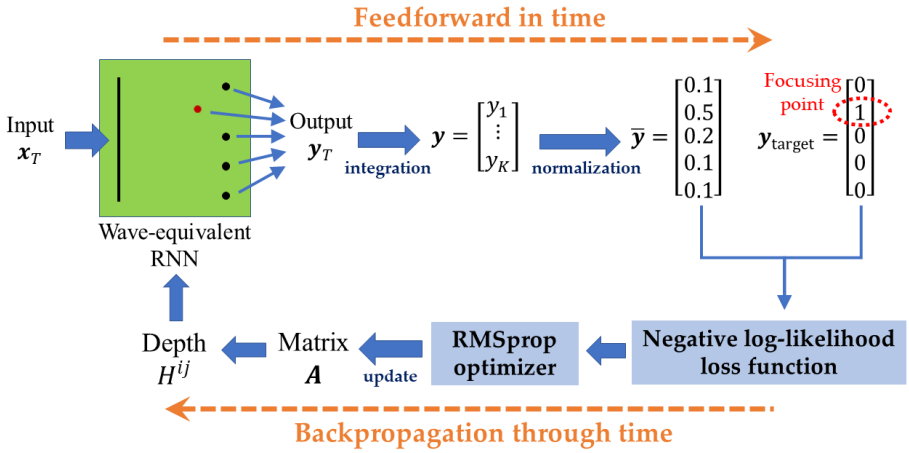

Figure 3. Illustration of the wave-equivalent RNN workflow for a training epoch.

The proposed training process fits in the paradigm of supervised learning: the objective is to learn an optimal bathymetry that directs incident waves (features/inputs) to a designed focusing location represented by a one-hot vector (label/target). The wave-focusing problem is effectively converted into a classification problem after defining the wave-equivalent RNN model. In a typical classification problem, the network is trained to output the correct classification predictions for the input data, while for wave focusing, the RNN is trained to distribute the input energy to the designed location, or in other words, to "classify" the input into the particular category that is specified by a designer. Figure 4 shows the snapshots of wave propagation over the optimized bathymetry computed by a trained wave-equivalent RNN, in which the circles are output probes.

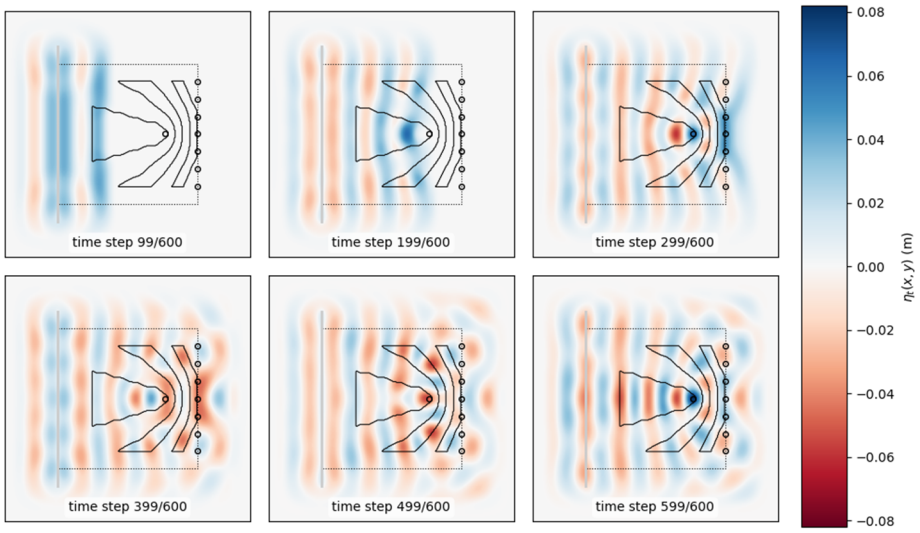

Figure 4. A series of snapshots of the wave field computed within a single training epoch.

3. Results and Discussion

3.1. Reflection and Refraction

Wave directing is achieved through different wave dynamics, such as reflection and refraction. Different wave-focusing bathymetry can be obtained by changing the arrangement of output probes and the selection of the focal point out of the probes. Six different cases are studied using the proposed RNN approach in this section, revealing the directing effects of reflection and refraction of shallow-water waves. Both the simplified shallow-water wave equation (Equation (9)) and the hyperbolic mild-slope equation (Equation (11)) are used to develop the equivalent RNN models for training.

In the first case, the focal point is placed at the midpoint of the front edge of the trained area, and other probes are placed evenly at the rear edge to prevent wave energy from passing through the trained area. Figure 5 shows (a) the final optimized bathymetry and the arrangement of probes; (b) the snapshot of wave elevation over the optimized bathymetry when maximum wave height occurs; and (c) the changing values of the loss function in training, all computed using the equivalent RNN model of Equation (9). The corresponding results computed using the equivalent model of Equation (11) are presented in Figure 6.

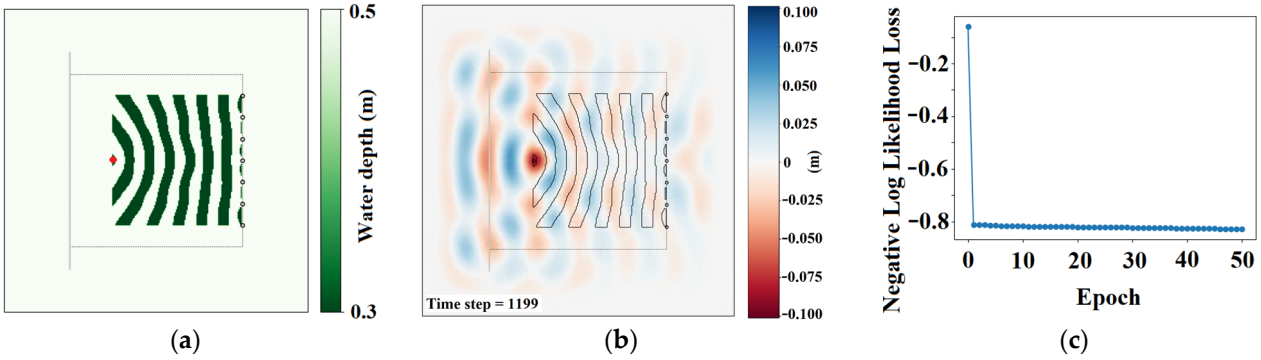

Figure 5. Results of the first case from the equivalent RNN model of Equation (9) (learning rate = 0.9): (**a**) optimized bathymetry with probes; (**b**) snapshot of wave elevation; (**c**) loss values of training.

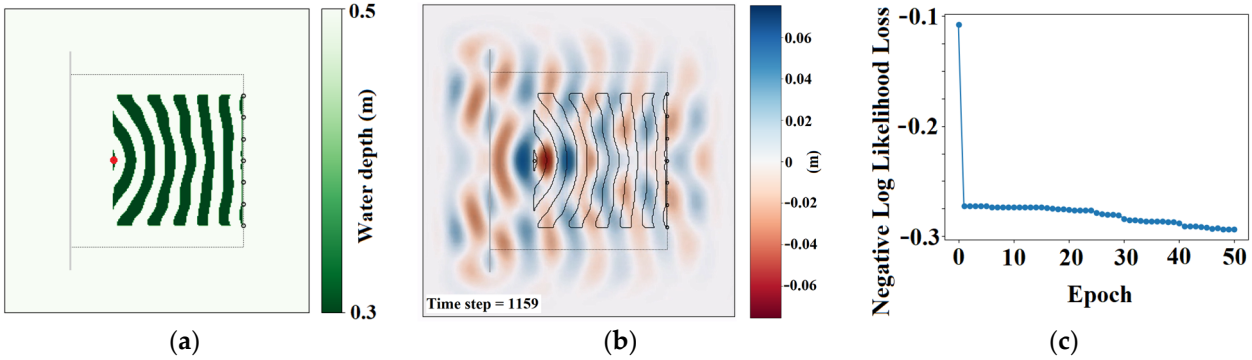

Figure 6. Results of the first case from the equivalent RNN model of Equation (11) (learning rate = 1.2): (**a**) optimized bathymetry with probes; (**b**) snapshot of wave elevation; (**c**) loss values of training.

For the first case, the final optimized topographies obtained, respectively, using the simplified equation and the mild-slope equation are nearly identical. Both topographies have curved strips, clearly implying the Bragg reflection and parabolic reflector phenomena. The interval distance between these stripe bulges is half of the incident wavelength. Although both equivalent RNN models produce optimized topographies that successfully reflect and focus wave energy to the designed target location, the mild-slope equation predicts a noticeably different wave field: the maximum wave height is exactly at the focal point for the simplified model (Figure 5b), while for the mild-slope model, the maximum wave height occurs at two locations near the selected focal point (Figure 6b). Therefore, the

final loss value of the simplified model is much smaller than that of the mild-slope model (Figure 5c vs. Figure 6c).

In the second case, the focal point is placed in the middle of the trained area. Figure 7 presents the results from the simplified model. Curved stripes exist behind the focal point to produce Bragg and parabolic reflection for wave focusing. An arrowhead-like bulge on the bottom appears in front of the focal point. This bathymetry feature guides the wave to the focal point via refraction and reflects the wave from the stripes back to the focal point. The final bathymetry optimized and wave propagation predicted by the mild-slope model are very similar to those of the simplified model.

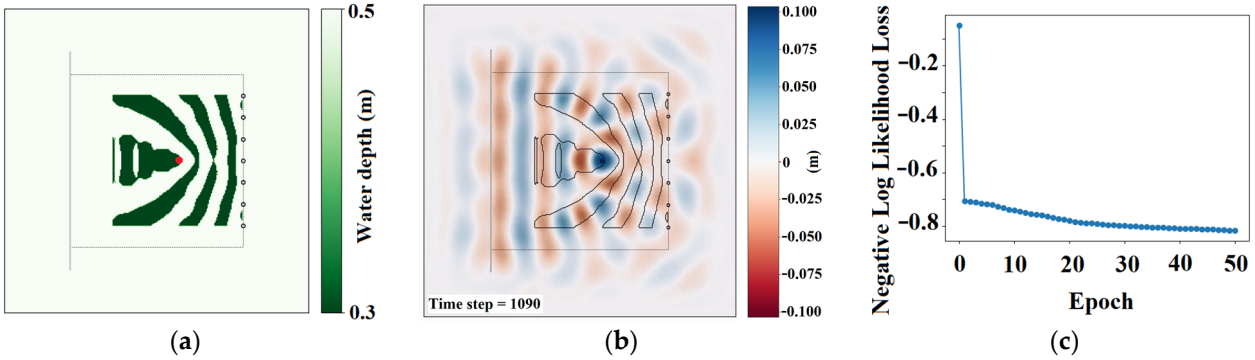

Figure 7. Results of the second case from the equivalent RNN model of Equation (9) (learning rate = 0.9): (**a**) optimized bathymetry with probes; (**b**) snapshot of wave elevation; (**c**) loss values of training.

In the third case, the focal point is selected as the midpoint of the rear edge, which implies that wave energy should pass the trained area only through the middle. Figures 8 and 9 show the results from the simplified and the mild-slope models, respectively. The final topographies optimized by the two different RNN models share the same general layout but with different details (Figure 8a vs. Figure 9a). The refraction effect plays a major role in wave directing, and no reflection stripe is found. As shown in Figures 8b and 9b, the incident wave bends and converges to the designed focusing location as it passes over the optimized bathymetry.

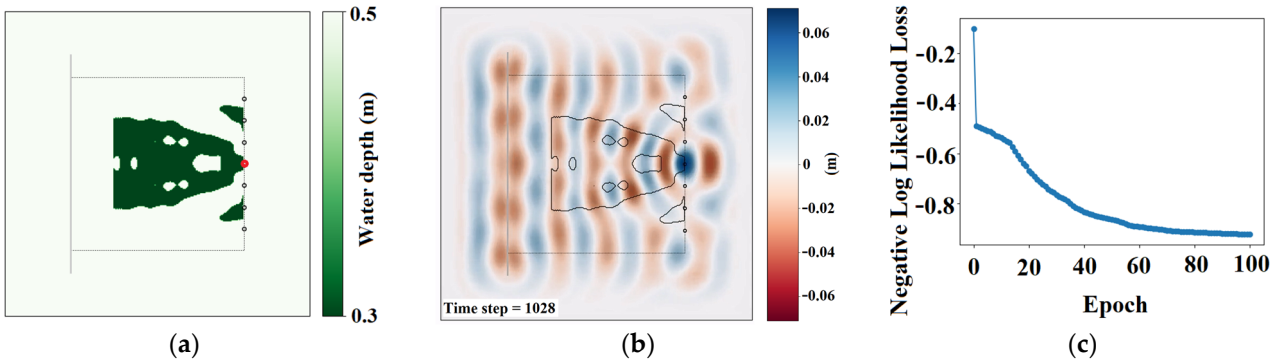

Figure 8. Results of the third case from the equivalent RNN model of Equation (9) (learning rate = 0.9): (**a**) optimized bathymetry with probes; (**b**) snapshot of wave elevation; (**c**) loss values of training.

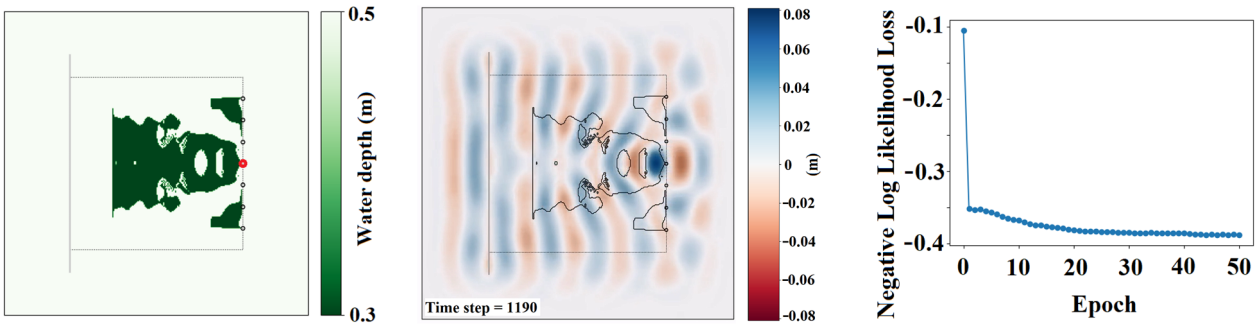

Figure 9. Results of the third case from the equivalent RNN model of Equation (11) (learning rate = 1.0): (**a**) optimized bathymetry with probes; (**b**) snapshot of wave elevation; (**c**) loss values of training.

To study how varying bathymetry redirects wave energy asymmetrically, the focal point is placed, respectively, at the start point, midpoint, and end point of the upper edge of the trained area in the fourth, fifth, and sixth cases. The results predicted by the simplified-equation RNN model and by the mild-slope-equation RNN model are essentially similar, and therefore, we only present the results from the mild-slope model in Figures 10–12 for the fourth, fifth, and sixth cases.

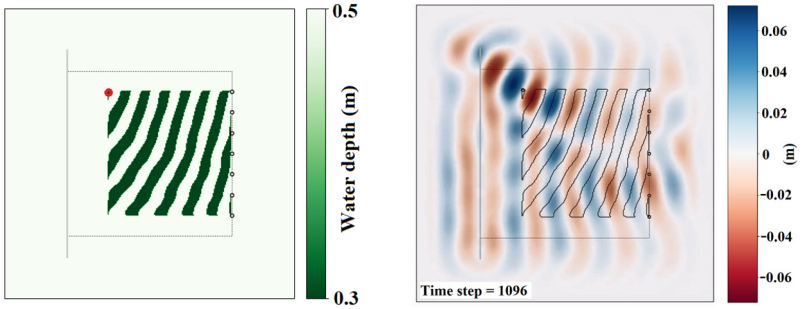

Figure 10. Results of the fourth case from the equivalent RNN model of Equation (11) (learning rate = 1.2): (**a**) optimized bathymetry with probes; (**b**) snapshot of wave elevation.

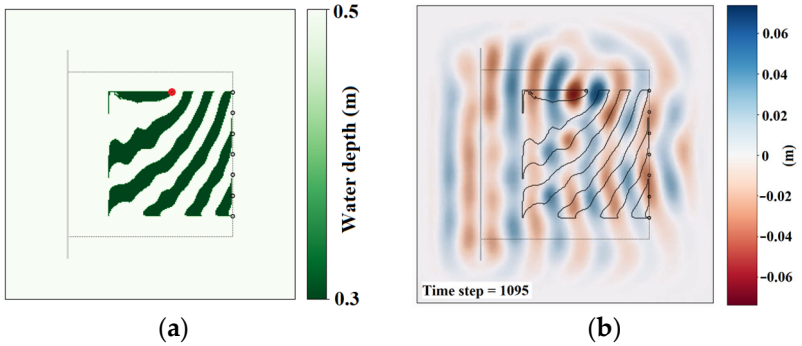

Figure 11. Results of the fifth case from the equivalent RNN model of Equation (11) (learning rate = 1.2): (**a**) optimized bathymetry with probes; (**b**) snapshot of wave elevation.

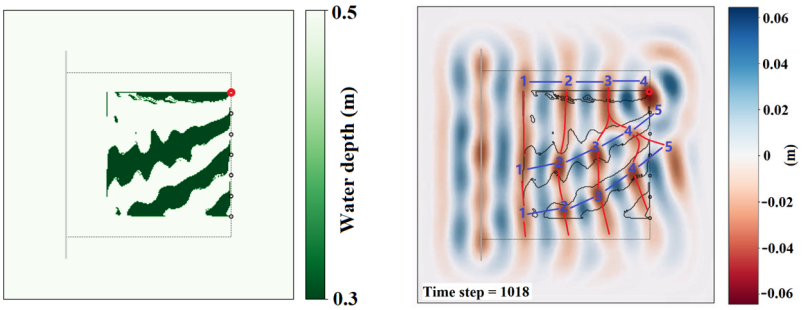

(**a**) (**b**)

Figure 12. Results of the sixth case from the equivalent RNN model of Equation (11) (learning rate = 1.2): (**a**) optimized bathymetry with probes; (**b**) snapshot of wave elevation.

The following observations were noticed from the results shown in Figures 10–12. Firstly, the optimized topographies successfully achieve wave focusing as designed. Secondly, for the fourth and fifth cases in which the reflection effect is dominant, the resulting topographies have curved stripe bulges similar to their symmetrical counterparts, the first and second cases. Lastly, the refraction effect is dominant in the sixth case but works differently compared to the third case: the curved stripe bulge slows down and guides the wave toward the focal point, where the guided wave merges with the incident wave with a phase delay of 2π (see the illustration in Figure 12b).

The effectiveness of wave energy focusing is compared for the six tested cases. The maximum wave height and the energy-focusing factor of the wave field over the optimized bathymetry are listed in Table 1. The energy focusing factor is computed as the ratio between the energy flux at the focusing location with the maximum wave height and the energy flux of the incident wave. The simplified shallow-water wave equation generally predicts a more significant wave-focusing result than the mild-slope equation, especially for reflection focusing, because the simplified equation rigorously conforms to Bragg's law. The topographies optimized using the proposed approach effectively converge wave energy to the designed locations. The maximum wave heights that appear at or near the target focal point are about 3 to 4 times as large as the incident wave height, resulting in energy fluxes that are around 8 to 15 times greater than the incident wave. The most significant focusing effect is observed when the target probe is placed in the middle of the trained area. The incident wave is reflected by the curved stripes behind the focal point, and the resulting reflected wave can be reflected again by the arrowhead-like bulge in the front, which forms an energy trap for shallow-water waves.

Table 1. Effectiveness of wave energy focusing.

Case	Focal Point	Model	Maximum Wave Height	Energy Focusing Factor
1st	middle-front	simplified equation mild-slope equation	0.203 m 0.152 m	16.5 9.24
2nd	middle	simplified equation mild-slope equation	0.208 m 0.185 m	17.3 13.7
3rd	middle-rear	simplified equation mild-slope equation	0.142 m 0.162 m	8.07 10.5
4th	upper-front	simplified equation mild-slope equation	0.172 m 0.144 m	11.8 8.29
5th	upper-middle	simplified equation mild-slope equation	0.176 m 0.148 m	12.4 8.76
6th	upper-rear	simplified equation mild-slope equation	0.145 m 0.132 m	8.41 6.97

3.2. Evolution of Bathymetry

The bathymetry in the trained area is updated after each training epoch and evolves to the final optimized result. In this section, we select the first and third cases in Section 3.1 as examples to show the evolution of bathymetry during the training process. Figure 13 shows the topographies of the first case updated after the 1st, 10th, and 50th training epochs computed using the simplified model. Similarly, Figures 14 and 15 present the evolution of the bathymetry in the third case trained by the simplified and mild-slope models, respectively.

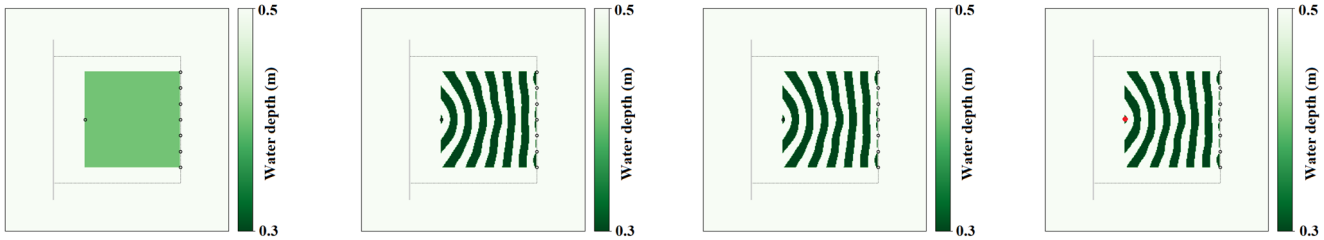

(**a**) epoch = 0 (initial) (**b**) epoch = 1 (**c**) epoch = 10 (**d**) epoch = 50

Figure 13. Evolution of bathymetry of the first case trained by the equivalent RNN model of Equation (9) with a learning rate of 0.9.

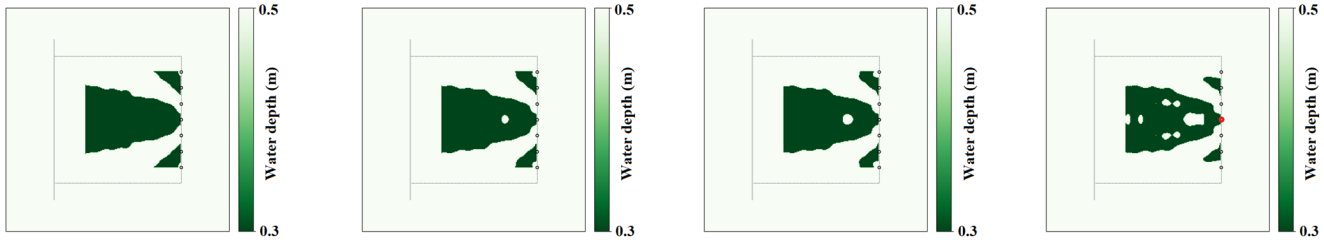

(**a**) epoch = 1 (**b**) epoch = 20 (**c**) epoch = 50 (**d**) epoch = 100

Figure 14. Evolution of bathymetry of the third case trained by the equivalent RNN model of Equation (9) with a learning rate of 0.9.

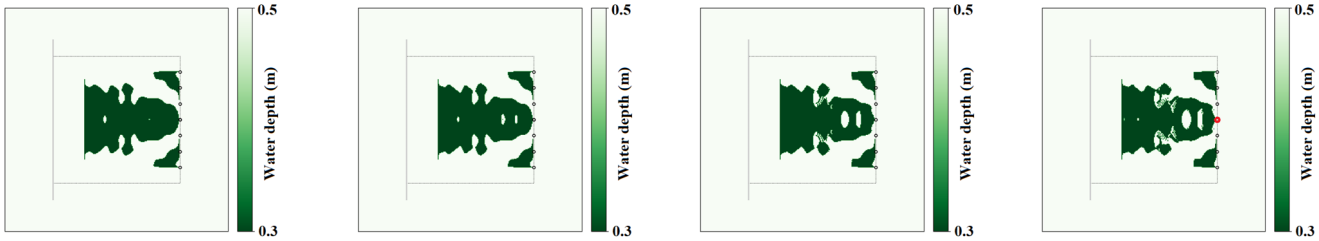

(**a**) epoch = 1 (**b**) epoch = 10 (**c**) epoch = 20 (**d**) epoch = 50

Figure 15. Evolution of bathymetry of the third case trained by the equivalent RNN model of Equation (11) with a learning rate of 1.0.

The proposed wave-equivalent RNN models work efficiently, and a relatively large learning rate (0.8 to 1.2) can be applied. Especially for reflection focusing, the bathymetry shows the curved stripe features and the loss value drops dramatically after just one training epoch (see Figures 5c, 6c and 13). For refraction focusing, the general layout of the optimized bathymetry is obtained just after the first epoch, but detailed configurations of the terrain take more training to appear (Figures 14 and 15).

3.3. Limitations and CFD Verifications

3.3.1. Limitations of the Proposed Method

The proposed machine learning method is subject to several limitations. First of all, the hydrodynamic effects considered are limited by the hydrodynamic model employed. The wave-equivalent RNN models in this work are developed, respectively, based on the simplified shallow-water wave equation and the mild-slope equation, and the resulting RNN models are linear without consideration of wave breaking or wave-induced current. Therefore, applications of these RNN models should conform to the assumptions of shallow water, small amplitude, and smooth topography. Secondly, the placement of the output probes is critical in the training process and requires the users to have a basic understanding of wave mechanics. The probes should spread evenly around the control wave field and the focusing probe must be placed at a physically possible location for wave focusing. For example, the training cannot converge if the focusing probe is placed far away from the trainable bathymetry or it is surrounded by other wave-canceling probes. The wave-equivalent RNN simply cannot provide an optimized result that is beyond the physics of the wave system. Third, the final bathymetry and/or the wave field optimized by the RNN model may not conform to the original assumptions because the wave system has been modified during the training process. For instance, the optimized topography may not be smooth or wave breaking might occur at the focusing point. Further verification or an upgrade of the RNN using a more advanced wave model should be considered for such scenarios.

Morphodynamic effects are neglected in the present method as we assume the spatially varying bathymetry is fixed in time. There are several implications of neglecting morphodynamic effects. First, the application of the present method to sandy or muddy seafloors requires further morphodynamic evaluation for long-term feasibility, because the bathymetry may evolve rapidly after construction and neutralize its design purpose. Second, the survivability of optimized bathymetry needs additional nonlinear hydrodynamic and morphodynamic modeling for extreme conditions, such as a tsunami or storm surge. Third, shoreline response to an optimized topography is not readily available in the present method due to the lack of morphodynamic modeling, which is critical for coastal protection applications.

In addition, constructing underwater topography on a large scale could be rather expensive. Although the scope of this paper is the technical feasibility of the proposed machine learning method, the economic feasibility is to be investigated in a real-world scenario.

3.3.2. CFD Numerical Wave Tank Verifications

In this study, we noticed that no wave breaking occurs because the wave steepness at the focusing location remains small for the small-amplitude incident wave. However, the optimized topographies have sharp edges, and the smooth topography assumption is no longer valid. Therefore, we developed a CFD numerical wave tank based on the FLOW-3D software to verify the wave-focusing effects of the optimized topographies and the effectiveness of the proposed approach. Three simulation cases were carried out for both reflection and refraction effects. The topographies optimized using the two equivalent RNN models are nearly identical in the first case of Section 3.1; therefore, we only employed the bathymetry in Figure 6a for CFD simulation to verify the reflection focusing effect. For the refraction effect, we selected the two topographies of the third case in Section 3.1, which were, respectively, optimized by the simplified and the mild-slope models.

Viscous fluid and the k-ω Reynolds-averaged Navier–Stokes turbulence model were employed in the CFD simulations to capture the effects of bottom friction and turbulence around the sharp edges. Figure 16 shows the configuration of the CFD wave tank and the bathymetry model of the first simulation case. The wave tank was 65 m (6.5L) in length, 20 m (2L) in width, and 0.8 m in height, including a water layer of 0.5 m and an air layer of 0.3 m. A damped zone was placed in the range between x = 55 m and x = 65 m with a damping coefficient of 5. The inlet boundary at x = 0 was a *wave* boundary, and an *outflow*

boundary was set at x = 65 m. The upper boundary at z = 0.8 m was set as a *specified pressure* boundary for the atmosphere, and the bottom at z = 0 was a non-slip *wall* boundary. Since the bathymetry is symmetrical, only half of the wave field was simulated using a *symmetry* boundary. The *Stokes and Cnoidal* option was selected for the *wave* boundary to generate the incident wave with a wave height of 0.05 m and a period of 4.588 s. The timestep size was fixed at 0.01 s. The grid sizes in the x, y, and z dimensions were 0.2 m, 0.2 m, and 0.02 m, respectively. A validation case was performed first without varying the bathymetry to test the generation of the incident wave (Figure 17), which matched well with the target shallow-water wave. Overlapping grids were applied to model the terrain of varying bathymetry, whose horizontal dimension was set to 0.05m based on the tests of convergency. The total number of grids, depending on the different bathymetry, was about 3 million for each case.

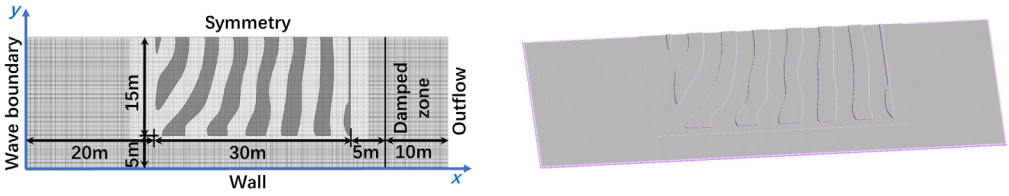

(**a**) (**b**)

Figure 16. Configuration of the CFD wave tank: (**a**) dimensions and boundaries; (**b**) model of varying bathymetry.

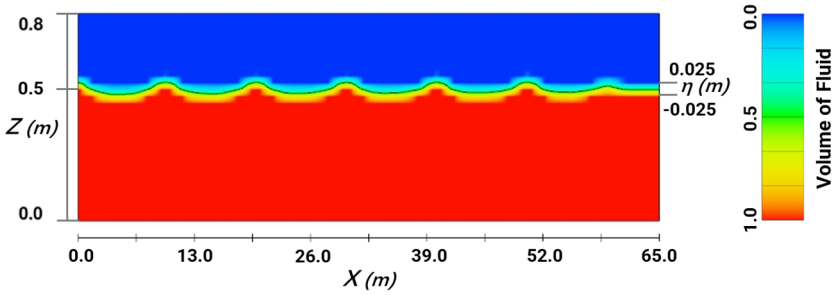

Figure 17. Validation of the incident wave without varying bathymetry.

For the first simulation case, Figures 18 and 19 show the wave field and the surface elevation in the symmetrical plane for two different timesteps, respectively. The maximum wave height observed in the simulation is 0.12 m, and it occurs on the center line at around x = 22.7 m. Two secondary focal points are also observed at x = 17.6 m and x = 27.2 m. Although the numerical simulations are computed based on a different wave theory and viscous fluid, the reflection focusing effect was successfully verified by the numerical wave tank experiments. The CFD simulation results are close to the prediction of the mild-slope equation, compared to Figures 5b and 6b.

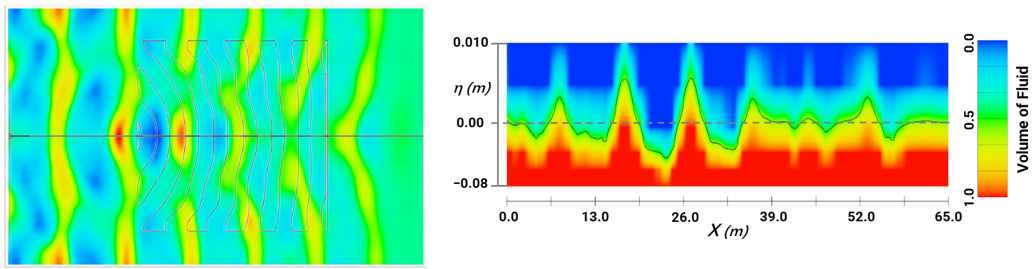

(**a**) (**b**)

Figure 18. Results of the first simulation case for timestep t = 76.42 s: (**a**) wave field of surface elevation; (**b**) surface elevation in the center vertical plane.

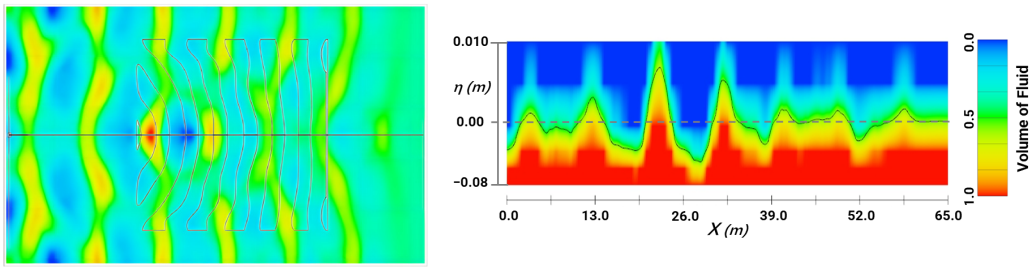

(**a**) (**b**)

Figure 19. Results of the first simulation case for timestep t = 78.99 s: (**a**) wave field of surface elevation; (**b**) surface elevation in the center vertical plane.

The results of the second and third simulation cases are presented in Figures 20 and 21, showing the moments when the highest wave peaks appear. The topographies optimized by the simplified and the mild-slope models are simulated, and both topographies demonstrate shallow-water wave focusing through the refraction effect at the location at x = 48 m $\sim$ 52 m on the center line. The bathymetry optimized by the simplified model yields a maximum wave height of 0.11 m, while the bathymetry optimized by the mild-slope model results in a maximum wave height of 0.10m. Comparing Figures 20a and 21a to Figures 9b and 10b, respectively, the mild-slope equation model predicts closer results to the CFD simulation.

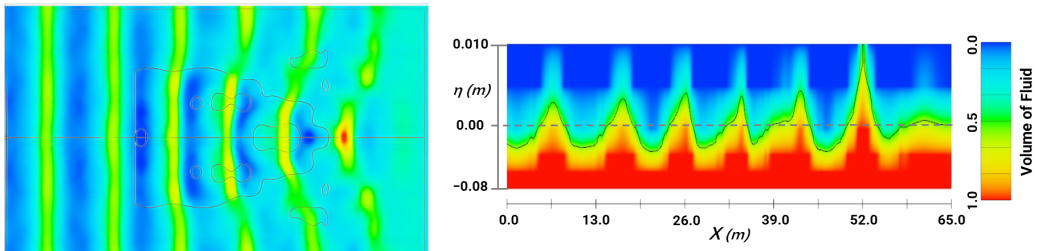

(**a**) (**b**)

Figure 20. Results of the second simulation case for timestep t = 57.60 s: (**a**) wave field of surface elevation; (**b**) surface elevation in the center vertical plane.

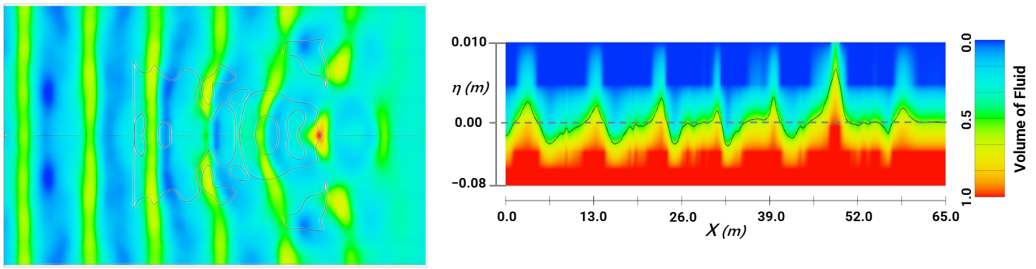

(**a**) (**b**)

Figure 21. Results of the third simulation case for timestep t = 65.01 s: (**a**) wave field of surface elevation; (**b**) surface elevation in the center vertical plane.

4. Conclusions

In this paper, we propose a novel machine learning approach to design and optimize spatially varying, temporally fixed bathymetry for directing shallow-water wave energy using wave-equivalent RNN. Two wave-equivalent RNN models were developed to embody the simplified shallow-water wave equation and the mild-slope equation, utilizing the mathematical mapping between wave dynamics and the computation of RNN. The wave-equivalent RNN models were trained with various training setups, and the training

results were analyzed and discussed. A CFD wave tank was also developed to verify the wave-focusing effect of the optimized topographies. The following main conclusions can be drawn from this study:

(1) Shallow-water waves can be effectively directed using varying bathymetry, in which Bragg reflection and refraction effects play important roles.
(2) Reflection generally offers better wave-focusing results than refraction.
(3) The mild-slope equation RNN model provides closer results to CFD simulations because the slopes of bathymetry are taken into account, compared to the simplified model.
(4) The equivalence between the dynamics of wave systems and the computation of RNN models offers a promising basis to develop intelligent machine learning tools for solving engineering problems.

As discussed in Section 3.3.1, the present method is subject to some limitations. Its applicability depends on the wave model used to develop the wave-equivalent RNN and its reliability relies on a proper setup of the output probes and the training target. Here, we highlight several possible extensions of the present study:

(1) More complicated equations of a shallow-water wave system can be applied to develop more accurate equivalent RNN models to improve real-world efficacy. For example, a Boussinesq-type wave model including the wave breaking and wave-induced current formulations can be applied for hydrodynamic modeling.
(2) A sediment transport module can be added into the wave system to enable morphodynamic modeling in the RNN, such that the bathymetry outside the trainable area (construction zone) can interact and evolve with wave motions.
(3) The output of the RNN model and the corresponding training target can be revised to serve various engineering purposes. For instance, the velocity or sediment concentration in the wave field can be defined as the output for the study of shoreline erosion.
(4) Irregular incident waves can be easily implemented without modification to the proposed approach.

Author Contributions: Conceptualization, S.T. and L.Z.; methodology, S.T.; software, S.T. and Y.Y.; validation, Y.Y. and L.Z.; formal analysis, S.T.; investigation, S.T.; resources, S.T. and L.Z.; data curation, S.T. and Y.Y.; writing—original draft preparation, S.T.; writing—review and editing, L.Z. and Y.Y.; visualization, S.T.; supervision, L.Z.; project administration, L.Z.; funding acquisition, S.T. and L.Z. All authors have read and agreed to the published version of the manuscript.

Funding: This research was funded by the National Natural Science Foundation of China (grant number 12102136); Guangdong Basic and Applied Basic Research Foundation (grant number 2020A1515110072); and Guangzhou Science and Technology Program (grant number 202102021013).

Data Availability Statement: Data will be made available on request.

Conflicts of Interest: The authors declare no conflict of interest.

References

1. Nordstrom, K.F. Living with shore protection structures: A review. *Estuar. Coast. Shelf Sci.* **2014**, *150*, 11–23. [CrossRef]
2. Schoonees, T.; Mancheño, A.G.; Scheres, B.; Bouma, T.J.; Silva, R.; Schlurmann, T.; Schüttrumpf, H. Hard structures for coastal protection, towards greener designs. *Estuaries Coasts* **2019**, *42*, 1709–1729. [CrossRef]
3. Morris, R.L.; Konlechner, T.M.; Ghisalberti, M.; Swearer, S.E. From grey to green: Efficacy of eco-engineering solutions for nature-based coastal defence. *Glob. Change Biol.* **2018**, *24*, 1827–1842. [CrossRef] [PubMed]
4. Amos, D.; Akib, S. A review of coastal protection using artificial and natural countermeasures—Mangrove vegetation and polymers. *Eng* **2023**, *4*, 941–953. [CrossRef]
5. Ranasinghe, R.; Turner, I.L. Shoreline response to submerged structures: A review. *Coast. Eng.* **2006**, *53*, 65–79. [CrossRef]
6. Na'im, I.I.; Shahrizal, A.R.M.; Safari, M.D. A Short Review of Submerged Breakwaters. *MATEC Web Conf.* **2018**, *203*, 01005.
7. Saengsupavanich, C.; Ariffin, E.H.; Yun, L.S.; Pereira, D.A. Environmental impact of submerged and emerged breakwaters. *Heliyon* **2022**, *8*, e12626. [CrossRef]
8. Bheeroo, V.A.; Yeh, H. Standing longwave formations in reef-lagoon bathymetries. *Coast. Eng.* **2021**, *168*, 103949. [CrossRef]
9. Bheeroo, V.A.; Yeh, H. Long-wave response to laterally periodic reef-lagoon bathymetry. *Coast. Eng.* **2022**, *178*, 104218. [CrossRef]

10. Pan, Y.; Tong, H.; Wei, D.; Xiao, W.; Xue, D. Review of structure types and new development prospects of artificial reefs in China. *Front. Mar. Sci.* **2022**, *9*, 853452. [CrossRef]
11. Li, C.Y.; Shih, R.S.; Weng, W.K. Visualization investigation of energy dissipation induced by eddy currents for a solitary-like wave passing over submerged breakwater sets. *J. Mar. Sci. Eng.* **2020**, *8*, 834. [CrossRef]
12. Patil, S.B.; Karmakar, D. Performance evaluation of submerged breakwater using multi-domain boundary element method. *Appl. Ocean Res.* **2021**, *114*, 102760. [CrossRef]
13. Xue, S.; Xu, Y.; Xu, G.; Wang, J.; Chen, Q. A novel tri-semicircle shaped submerged breakwater for mitigating wave loads on coastal bridges part I: Efficacy. *Ocean Eng.* **2022**, *245*, 110462. [CrossRef]
14. Jafarzadeh, E.; Bohluly, A.; Kabiri-Samani, A.; Mansourzadeh, S. A study on the performance of circular and rectangular submerged breakwaters using nun-uniform FGVT method. *Coast. Eng. J.* **2023**, *65*, 2170688. [CrossRef]
15. Atras, M.F.; Lalang, R.; Magdalena, I. Optimal sinusoidal submerged breakwater for coastal protection. *AIP Conf. Proc.* **2021**, *2423*, 020022.
16. Brancasi, A.; Leone, E.; Francone, A.; Scaravaglione, G.; Tomasicchio, G.R. On formulae for wave transmission at submerged and low-crested breakwaters. *J. Mar. Sci. Eng.* **2022**, *10*, 1986. [CrossRef]
17. Gallerano, F.; Cannata, G.; Palleschi, F. Hydrodynamic effects produced by submerged breakwaters in a coastal area with a curvilinear shoreline. *J. Mar. Sci. Eng.* **2019**, *7*, 337. [CrossRef]
18. Kuang, C.; Ma, Y.; Han, X.; Pan, S.; Zhu, L. Experimental observation on beach evolution process with presence of artificial submerged sand bar and reef. *J. Mar. Sci. Eng.* **2020**, *8*, 1019. [CrossRef]
19. Ranasinghe, R.S. Modelling of waves and wave-induced currents in the vicinity of submerged structures under regular waves using nonlinear wave-current models. *Ocean Eng.* **2022**, *247*, 110707. [CrossRef]
20. Bouvier, C.; Castelle, B.; Balouin, Y. Modeling the impact of the implementation of a submerged structure on surf zone sandbar dynamics. *J. Mar. Sci. Eng.* **2019**, *7*, 117. [CrossRef]
21. Vieira, B.F.V.; Pinho, J.L.S.; Barros, J.A.O.; Carmo, J.S. Hydrodynamics and morphodynamics performance assessment of three coastal protection structures. *J. Mar. Sci. Eng.* **2020**, *8*, 175. [CrossRef]
22. da Silva, R.F.; Hansen, J.E.; Rijnsdorp, D.P.; Lowe, R.J.; Buckley, M.L. The influence of submerged coastal structures on nearshore flows and wave runup. *Coast. Eng.* **2022**, *177*, 104194. [CrossRef]
23. Couston, L.-A.; Jalali, M.A.; Alam, M.-R. Shore protection by oblique seabed bars. *J. Fluid Mech.* **2017**, *815*, 481–510. [CrossRef]
24. Fox, B.N.; Gomes, R.P.F.; Gato, L.M.C. Analysis of oscillating-water-column wave energy converter configurations for integration into caisson breakwaters. *Appl. Energy* **2021**, *295*, 117023. [CrossRef]
25. Deng, Z.; Wang, P.; Cheng, P. Hydrodynamic performance of an asymmetry OWC device mounted on a box-type breakwater. *Front. Mar. Sci.* **2021**, *8*, 677030. [CrossRef]
26. Zhou, B.; Zheng, Z.; Jin, P.; Wang, L.; Zang, J. Wave attenuation and focusing performance of parallel twin parabolic arc floating breakwaters. *Energy* **2022**, *260*, 125164. [CrossRef]
27. Abanades, J.; Flor-Blanco, G.; Flor, G.; Iglesias, G. Dual wave farms for energy production and coastal protection. *Ocean Coast. Manag.* **2018**, *160*, 18–29. [CrossRef]
28. Deng, Z.; Wang, C.; Yao, Y.; Higuera, P. Numerical simulation of an oscillating water column device installed over a submerged breakwater. *J. Mar. Sci. Technol.* **2019**, *25*, 258–271. [CrossRef]
29. Zhang, H.; Tao, A.; Tu, J.; Su, J.; Xie, S. The focusing waves induced by Bragg resonance with V-shaped undulating bottom. *J. Mar. Sci. Eng.* **2021**, *9*, 708. [CrossRef]
30. Li, B. An evolution equation for water waves. *Coast. Eng.* **1994**, *23*, 227–242. [CrossRef]
31. Chamberlain, P.G.; Porter, D. The modified mild-slope equation. *J. Fluid Mech.* **1995**, *291*, 393–407. [CrossRef]
32. Porter, D.; Staziker, D.J. Extensions of the mild-slope equation. *J. Fluid Mech.* **1995**, *300*, 367–382. [CrossRef]
33. Suh, K.-D.; Lee, C.; Park, W.S. Time-dependent equations for wave propagation on rapidly varying topography. *Coast. Eng.* **1997**, *32*, 91–117. [CrossRef]
34. Lee, C.; Kim, G.; Suh, K.-D. Extended mild-slope equation for random waves. *Coast. Eng.* **2003**, *48*, 277–287. [CrossRef]
35. Schäffer, H.A.; Madsen, P.A. Further enhancements of Boussinesq-type equations. *Coast. Eng.* **1995**, *26*, 1–14. [CrossRef]
36. Beji, S.; Nadaoka, K. A formal derivation and numerical modelling of the improved Boussinesq equations for varying depth. *Ocean Eng.* **1996**, *23*, 604–691. [CrossRef]
37. Madsen, P.A.; Schäffer, H.A. Higher-order Boussinesq-type equations for surface gravity waves—Derivation and analysis. *Philos. Trans. R. Soc. London. Ser. A Math. Phys. Eng. Sci.* **1998**, *356*, 3123–3184. [CrossRef]
38. Zou, Z.L. High order Boussinesq equations. *Ocean Eng.* **1999**, *26*, 767–792. [CrossRef]
39. Zou, Z.L. A new form of higher order Boussinesq equations. *Ocean Eng.* **2000**, *27*, 557–575. [CrossRef]
40. Gobbi, M.F.; Kirby, J.T.; Wei, G.E. A fully nonlinear Boussinesq model for surface waves. Part 2. Extension to $O(kh)^4$. *J. Fluid Mech.* **2000**, *405*, 181–210. [CrossRef]
41. Madsen, P.A.; Fuhrman, D.R.; Wang, B. A Boussinesq-type model for fully nonlinear waves interacting with a rapidly varying bathymetry. *Coast. Eng.* **2006**, *53*, 487–504. [CrossRef]
42. Gao, J.; Zhou, X.; Zhou, L.; Zang, J.; Chen, H. Numerical investigation on effects of fringing reefs on low-frequency oscillations within a harbor. *Ocean Eng.* **2019**, *172*, 86–95. [CrossRef]

43. Gao, J.; Ma, X.; Dong, G.; Zang, J.; Zhou, X.; Zhou, L. Topographic influences on transient harbor oscillations excited by N-waves. *Ocean Eng.* **2019**, *192*, 106548. [CrossRef]
44. Yu, J.; Howard, L.N. On higher order Bragg resonance of water waves by bottom corrugations. *J. Fluid Mech.* **2010**, *659*, 484–504. [CrossRef]
45. Tao, A.; Yan, J.; Wang, Y.; Zheng, J.; Fan, J.; Qin, C. Wave power focusing due to the Bragg resonance. *China Ocean Eng.* **2017**, *31*, 458–465. [CrossRef]
46. Elandt, R.B.; Shakeri, M.; Alam, M.-R. Surface gravity-wave lensing. *Phys. Rev. E* **2014**, *89*, 023012. [CrossRef]
47. Gao, J.; Ma, X.; Dong, G.; Chen, H.; Liu, Q.; Zang, J. Investigation on the effects of Bragg reflection on harbor oscillations. *Coast. Eng.* **2021**, *170*, 103977. [CrossRef]
48. Hao, J.; Li, J.; Liu, S.; Wang, L. Wave amplification caused by Bragg resonance on parabolic-type topography. *Ocean Eng.* **2022**, *244*, 110442. [CrossRef]
49. Liu, H.-W. An approximate law of Class I Bragg resonance of linear shallow-water waves excited by five types of artificial bars. *Ocean Eng.* **2023**, *267*, 113245. [CrossRef]
50. Sherwood, C.R.; van Dongeren, A.; Doyle, J.; Hegermiller, C.A.; Hsu, T.-J.; Kalra, T.S.; Olabarrieta, M.; Penko, A.M.; Rafati, Y.; Roelvink, D.; et al. Modeling the morphodynamics of coastal response to extreme events: What shape are we in? *Annu. Rev. Mar. Sci.* **2022**, *14*, 457–492. [CrossRef]
51. Nicholson, J.; Broker, I.; Roelvink, J.; Price, D.; Tanguy, J.; Moreno, L. Intercomparison of coastal area morphodynamic models. *Coast. Eng.* **1997**, *31*, 97–123. [CrossRef]
52. Karambas, T.V. 2DH non-linear dispersive wave modelling and sediment transport in the nearshore zone. In *Coastal Engineering*; American Society of Civil Engineers: Reston, VA, USA, 1998; pp. 2940–2953.
53. Roelvink, J.A. Coastal morphodynamic evolution techniques. *Coast. Eng.* **2006**, *53*, 277–287. [CrossRef]
54. Rijn, L.C.V.; Ribberink, J.S.; Werf, J.V.D.; Walstra, D.J. Coastal sediment dynamics: Recent advances and future research needs. *J. Hydraul. Res.* **2013**, *51*, 475–493. [CrossRef]
55. Marino, M.; Faraci, C.; Musumeci, R.E. Shoaling waves interacting with an orthogonal current. *J. Mar. Sci. Eng.* **2020**, *8*, 281. [CrossRef]
56. Faraci, C.; Musumeci, R.E.; Marino, M.; Ruggeri, A.; Carlo, L.; Jensen, B.; Foti, E.; Barbaro, G.; Elsaßer, B. Wave- and current-dominated combined orthogonal flows over fixed rough beds. *Cont. Shelf Res.* **2021**, *220*, 104403. [CrossRef]
57. Ozkan, C.; Perez, K.; Mayo, T. The impacts of wave energy conversion on coastal morphodynamics. *Sci. Total Environ.* **2020**, *712*, 136424. [CrossRef] [PubMed]
58. Franzen, M.O.; Fernandes, E.H.L.; Siegle, E. Impacts of coastal structures on hydro-morphodynamic patterns and guidelines towards sustainable coastal development: A case studies review. *Reg. Stud. Mar. Sci.* **2021**, *44*, 101800. [CrossRef]
59. Goldstein, E.B.; Coco, G.; Plant, N.G. A review of machine learning applications to coastal sediment transport and morphodynamics. *Earth-Sci. Rev.* **2019**, *194*, 97–108. [CrossRef]
60. Russakovsky, O.; Deng, J.; Su, H.; Krause, J.; Satheesh, S.; Ma, S.; Huang, Z.; Karpathy, A.; Khosla, A.; Bernstein, M.; et al. Imagenet large scale visual recognition challenge. *Int. J. Comput. Vis.* **2015**, *115*, 211–252. [CrossRef]
61. Sutskever, I.; Vinyals, O.; Le, Q.V. Sequence to sequence learning with neural networks. In Proceedings of the 27th International Conference on Neural Information Processing Systems, NIPS, Montreal, QC, Canada, 8–13 December 2014; Volume 2, pp. 3104–3112.
62. Bento, P.M.R.; Pombo, J.A.N.; Mendes, R.P.G.; Calado, M.R.A.; Mariano, S.J.P.S. Ocean wave energy forecasting using optimized deep learning neural networks. *Ocean Eng.* **2021**, *219*, 108372. [CrossRef]
63. Zhu, K.; Shi, H.; Han, M.; Cao, F. Layout study of wave energy converter arrays by an artificial neural network and adaptive genetic algorithm. *Ocean Eng.* **2022**, *260*, 112072. [CrossRef]
64. Lin, W.; Shanab, B.H.; Lenderink, C.; Zuo, L. Multi-objective optimization of the buoy shape of an ocean wave energy converter using neural network and genetic algorithm. *IFAC-PapersOnLine* **2022**, *55*, 145–150. [CrossRef]
65. Cuadra, L.; Salcedo-Sanz, S.; Nieto-Borge, J.C.; Alexandre, E.; Rodriguez, G. Computational intelligence in wave energy: Comprehensive review and case study. *Renew. Sustain. Energy Rev.* **2016**, *58*, 1223–1246. [CrossRef]
66. Gu, C.; Li, H. Review on deep learning research and applications in wind and wave energy. *Energies* **2022**, *15*, 1510. [CrossRef]
67. Hughes, T.W.; Williamson, I.A.D.; Minkov, M.; Fan, S. Wave physics as an analog recurrent neural network. *Sci. Adv.* **2019**, *5*, eaay6946. [CrossRef]
68. PyTorch Documentation. Available online: https://pytorch.org/docs/stable/index.html (accessed on 12 December 2022).